

Remotely pumped GHz antibunched emission from single exciton centers in GaAs

Mingyun Yuan,^{*,†} Klaus Biermann,[†] Shintaro Takada,[‡] Christopher Bäuerle,[¶] and
Paulo V. Santos[†]

[†]*Paul-Drude-Institut für Festkörperelektronik, Leibniz-Institut im Forschungsverbund Berlin
e.V., Hausvogteiplatz 5-7, 10117 Berlin, Germany*

[‡]*National Institute of Advanced Industrial Science and Technology (AIST), National
Metrology Institute of Japan (NMIJ), 1-1-1 Umezono, Tsukuba, Ibaraki 305-8563, Japan*

[¶]*Univ. Grenoble Alpes, CNRS, Grenoble INP, Institut Néel, 38000 Grenoble, France*

E-mail: yuan@pdi-berlin.de

Abstract

Quantum communication networks require on-chip transfer and manipulation of single particles as well as their interconversion to single photons for long-range information exchange. Flying excitons propelled by GHz surface acoustic waves (SAWs) are outstanding messengers to fulfill these requirements. Here, we demonstrate the acoustic manipulation of single exciton centers consisting of individual excitons bound to shallow impurity centers embedded in a semiconductor quantum well. Time-resolved photoluminescence studies show that the emission intensity and energy from these centers oscillate at the SAW frequency of 3.5 GHz. Furthermore, these centers can be remotely pumped via acoustic transport of flying excitons along a quantum well channel over several microns. Time correlation studies reveal that the centers emit anti-bunched light, thus acting as single-photon sources operating at GHz frequencies. Our results

pave the way for the exciton-based on-demand manipulation and on-chip transfer of single excitons at microwave frequencies with a natural photonic interface.

Keywords

impurity centers, excitons, surface acoustic waves, remote pumping, single-photon sources, GHz microwave

Introduction

Flying photonic qubits are particularly interesting for quantum communication since the photon coherence can be preserved over several kilometers.¹ Photons are thus ideal particles for the implementation of quantum functionalities such as entanglement, non-localization and teleportation.^{2,3} The technical challenges associated with the manipulation of photonic states are, however, formidable due to the difficulty of bringing two photons into interaction within a short distance. Opto-electronic excitations in the solid state are, in contrast, much easier to manipulate. Here, promising candidates are flying opto-electronic qubits, which can be used for the exchange of quantum information between remote sites.⁴ Recently, flying qubits based on hybrid surface acoustic wave (SAW) structures on semiconductor platforms are attracting increasing attention.⁵ One prominent advantage of SAWs is the ability to provide mobile strain and piezoelectric potentials to modulate, confine, and transfer particles between remote on-chip locations. Researchers have coupled SAWs to a variety of systems, including, for example, self-assembled quantum dots,⁶⁻⁸ nanowires,^{9,10} electrons,¹¹⁻¹³ superconducting qubits,^{14,15} diamond NV centers,^{16,17} defect centers in SiC,¹⁸ and excitons.¹⁹⁻²² SAWs of μm -sized wavelengths have also been used to populate two-level systems with charged carriers as well as to induce the emission of anti-bunched photons at microwave frequencies.²³⁻²⁵ Finally, it has recently been demonstrated that SAWs can effectively manipulate and transport spin-polarized carriers in semiconductor structures²⁶⁻²⁸ down to the single particle level,^{29,30} a

further prerequisite for quantum information processing using flying particles.

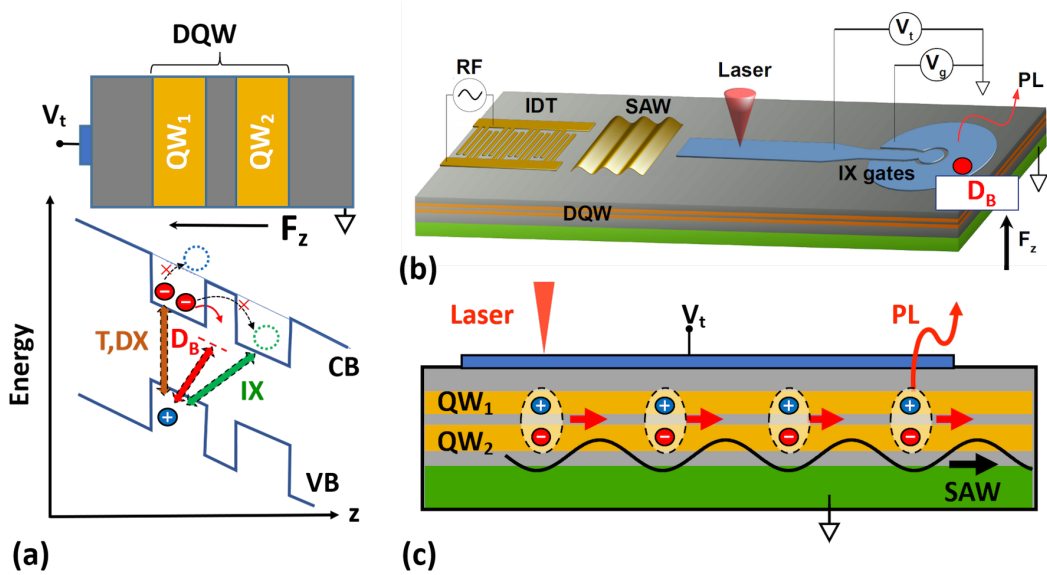


Figure 1: **Acoustic manipulations and transport of indirect excitons (IXs).** (a) IX formation via the dissociation of direct excitons (DXs) or trions (Ts) by the electric-field (F_z) induced electron tunneling between the quantum wells (QWs) of a double quantum well (DQW). For appropriate F_z values, the T or DX dissociation into IXs (dashed circles) can be blocked, leading to the selective excitation of bound exciton centers (D_B). (b) and (c) Sketches of the samples for acoustic IX transport. The IX are formed in the DQW regions underneath a stripe-like semitransparent gate subjected to a bias V_t , which enables both electrical control and optical access to the DQW. The stripe ends in a small circular trap area with a guard gate biased by V_g . An interdigital transducer (IDT) launches a SAW, which captures and transports the optically excited IXs along the stripe. The IX distribution is probed by collecting the spatially resolved photoluminescence (PL) along the path.

Flying excitons, with their natural inter-conversion to photons, offer several advantages for opto-electronic control as well as for interfacing electronic and photonic excitations. Especially suitable for the opto-electronic applications are the long-living spatially indirect (or dipolar) excitons (IXs) in a double quantum well (DQW) structure subjected to a transverse electric field F_z [cf. Fig 1(a)]. These excitons are formed by the Coulomb binding of electrons and holes driven to different quantum wells (QWs) by the applied field, which controls both the lifetime and the emission energy of the IXs via the quantum confined Stark effect. Single IXs can be isolated in small potential traps,³¹ as well as in single defect centers³² that act as sources of single-photons. Analogously to the acoustic transport of charged particles by the

SAW piezoelectric field,³³ the charge-neutral IXs have a long lifetime and can be confined and transported by the mobile band-gap modulation produced by the SAW strain field,¹⁹ as illustrated in Figs. 1(b) and 1(c). These interesting properties make flying IXs propelled by SAW fields potential candidates to complement the functionalities of single electrons in nano-electronic circuits requiring an interface to photons.

A main challenge for the implementation of flying excitonic qubits is the creation of two-level excitonic states interconnected by a transport channel, which can store single particles and convert them to photons. The long-range transport of IXs enabled by their long lifetime has so far only been demonstrated in wide transport channels using SAWs with wavelengths of a few μm .¹⁹⁻²¹ In this work, we realize a major step towards this goal by demonstrating the manipulation and remote pumping of single exciton centers by flying IXs propelled by GHz-SAWs in a GaAs-based semiconductor platform. The single centers used here consist of excitons bound to single shallow impurities (denoted as D_B) in a DQW structure. We have recently reported that these centers can be spectrally isolated and resonantly excited by appropriately biasing the DQW structure.³² Here, we demonstrate the pumping of individual D_B centers by IXs driven along a narrow transport channel by a SAW. The oscillating SAW strain field modulates the narrow emission lines of the D_B centers, which can be used as a sensitive probe of the local strain amplitudes. Time-resolved spectroscopic studies show that the recombination lifetime of the D_B states is sufficiently short to follow the 3.5 GHz SAW pumping rate. More importantly, photon correlation investigations reveal that the acoustic pumping of these centers is followed by the emission of anti-bunched photons with a repetition rate corresponding to the SAW frequency, which shows that the center acts as a single photon source operating at very high frequencies.

Results and discussion

Exciton energy modulation by SAWs

The D_B centers can be resonantly activated under weak optical excitation by biasing the DQW structure with a voltage V_t close to the onset of IX formation.³² Under these conditions, the photoexcited electron-hole pairs bind to free residual carriers to form trions (Ts). The conversion of trions to IXs via electron tunneling through the DQW barrier requires the excitation of a free electron to the band states. As illustrated in Fig. 1(a) the tunneling to single D_B becomes energetically favorable to the IX formation. The emission from these centers is characterized by a narrow line [with full-width-at-half-maximum (FWHM) of 0.2 meV, cf. lowest spectrum in Figure 2(a)] spectrally isolated from the IX and direct exciton (DX , excitons whose electron and hole reside in the same QW) transitions.

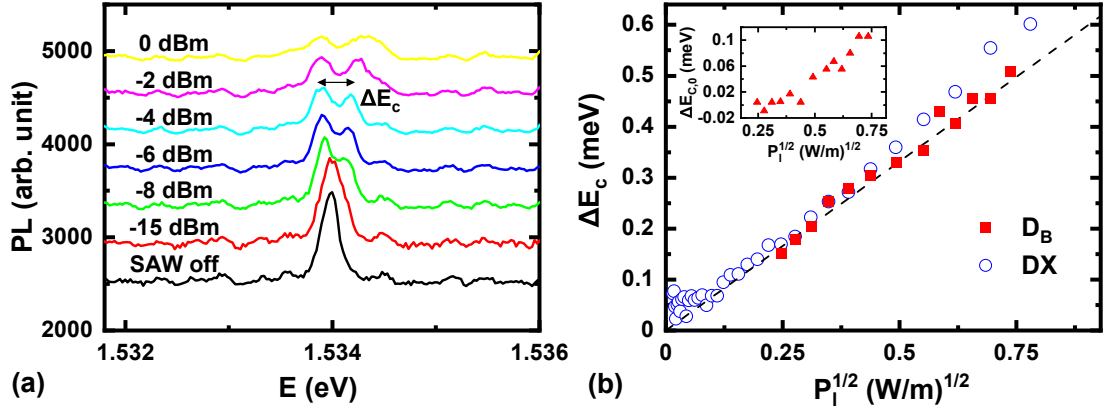


Figure 2: **Acoustic energy modulation of D_B centers** (a) Time-averaged photoluminescence (PL) spectra recorded for different acoustic power under local excitation. (b) Transition energy modulation amplitudes ΔE_B (red squares) and ΔE_{DX} (circles) as a function of the SAW power density. The dashed line yields the corresponding modulation determined from the model in the Supporting Information Sec. S1. Inset: power dependence of the central energy shift, $\Delta E_{C,0}$.

The spectroscopic studies were carried out with the setup of Figs. 1(b) and 1(c) using SAWs with a wavelength of $\lambda_{SAW} = 800$ nm (corresponding to a frequency of $f_{SAW} = 3.58$ GHz). The photoluminescence (PL) spectra of Fig. 2(a) show that under an increasing

SAW field the D_B line initially broadens and eventually splits into two. Here, the laser excitation spot coincided with the location of the D_B center within the spatial resolution (i.e. local excitation). The SAW strain field periodically modulates the excitonic transition energies $E_C(t)$ ($C = DX, T, D_B$) according to:³⁴

$$E_C(t) = E_{C,0} + \frac{\Delta E_C}{2} \sin\left(\frac{2\pi}{T_{\text{SAW}}}t\right), \quad (1)$$

where ΔE_C is the peak-to-peak modulation amplitude and $T_{\text{SAW}} = 1/f_{\text{SAW}}$ the SAW period.

For energy shifts ΔE_C smaller than the linewidth, the modulation manifests itself as an apparent broadening of the time-integrated PL lines. For larger modulation amplitudes, the time-averaged PL develops a camel-like shape with peaks at energies $E_{C,0} \pm \Delta E_C/2$ corresponding to the maximum and minimum band-gaps under the SAW field, thus, leading to the behavior observed in Fig. 2(a). At sufficiently high power the piezoelectric field from the SAW quenches the PL, as evident in the top curves in Fig. 2(a). Figure 2(b) displays the dependence of the peak-to-peak modulation amplitude for the D_B (ΔE_B) and DX (ΔE_{DX}) transitions determined from fits of the measured spectra to a model for the time-integrated PL line shape under a SAW described in detail in the Supporting Information (SI) Sec. S2. The dashed line yields the corresponding strain-induced band-gap modulation determined using the GaAs deformation potentials and the SAW fields in the DQW calculated from the applied rf-power (cf. Sec. S1). As expected for a shallow center, the D_B energy modulation amplitude follows closely the one for the DX states, which increases proportionally to the SAW amplitude (and, thus, to $\sqrt{P_\ell}$, P_ℓ being the linear power density of the SAW). It is worthwhile to emphasize that the narrow linewidth of D_B enables the quantitative determination of very small strain levels.

The central energy $E_{C,0}$ of the SAW-split D_B line in Fig. 2(a) also slightly blueshifts with increasing acoustic powers, as illustrated in the inset of Fig. 2(b). The shift $\Delta E_{C,0}$ is attributed to changes in the static field F_z caused by charge redistribution within the structure by the SAW piezoelectric field. This effect is nevertheless smaller compared to the

splitting ΔE_B caused by the SAW strain fields [see Figure 2(b) inset].

Long-range indirect exciton transport

The lower panel of Fig. 3(a) displays a spectrally resolved PL map of the exciton distribution under the electrostatic stripe gates under optical excitation by a focused laser spot at $y = 0$ [cf. sketch of Fig. 3(e)]. This map was recorded in the absence of a SAW under a transverse field $F_z = 5$ kV/cm applied across the DQW. The PL around the excitation spot (blue dotted line in the upper panel, integrated for $|y| < 3$ μm) shows the characteristic emission lines from the DXs, Ts, and IXs superimposed on a broad PL background from the doped layers and emission centers in the substrate (note that the intensity of the DX and T lines becomes strongly suppressed under the applied transverse field). Away from the generation area the PL becomes dominated by the emission from IXs, which, due to the long recombination lifetime, can diffuse up to the top region of the guard gate (thick orange line). In fact, most of the remote PL from DXs and Ts arises not from the diffusion of these species but rather from the conversion of diffusing IXs to DXs or Ts. Note also that the diffusing IXs can easily cross the narrow gap between the stripe and guard gate at $y = 13$ μm .

Figure 3(b) displays a PL map recorded under the same conditions as in Fig. 3(a), but now under a SAW propagating along the y direction. The acoustic field pushes the IXs upwards leading to a strong increase of the IX PL for positive y (cf. orange line in the upper panel) and a reduction for negative y . The recombination energy and location of the transported IXs can be controlled by changing the bias applied to the gates. As an example, Fig. 3(c) shows a map recorded by increasing the guard bias by 0.08 V relative to V_t . The IX emission energy blueshifts as IXs enter the guard gate due to the reduced F_z underneath the guard gate. Afterwards, they are pushed by the SAW beyond the guard, where they become converted to DXs or trions. The additional energy required to overcome the barrier between DXs (or Ts) and IXs is provided by the moving SAW field.

The IX transport over tens of λ_{SAW} can remotely activate D_B , as shown in Fig. 3(d).

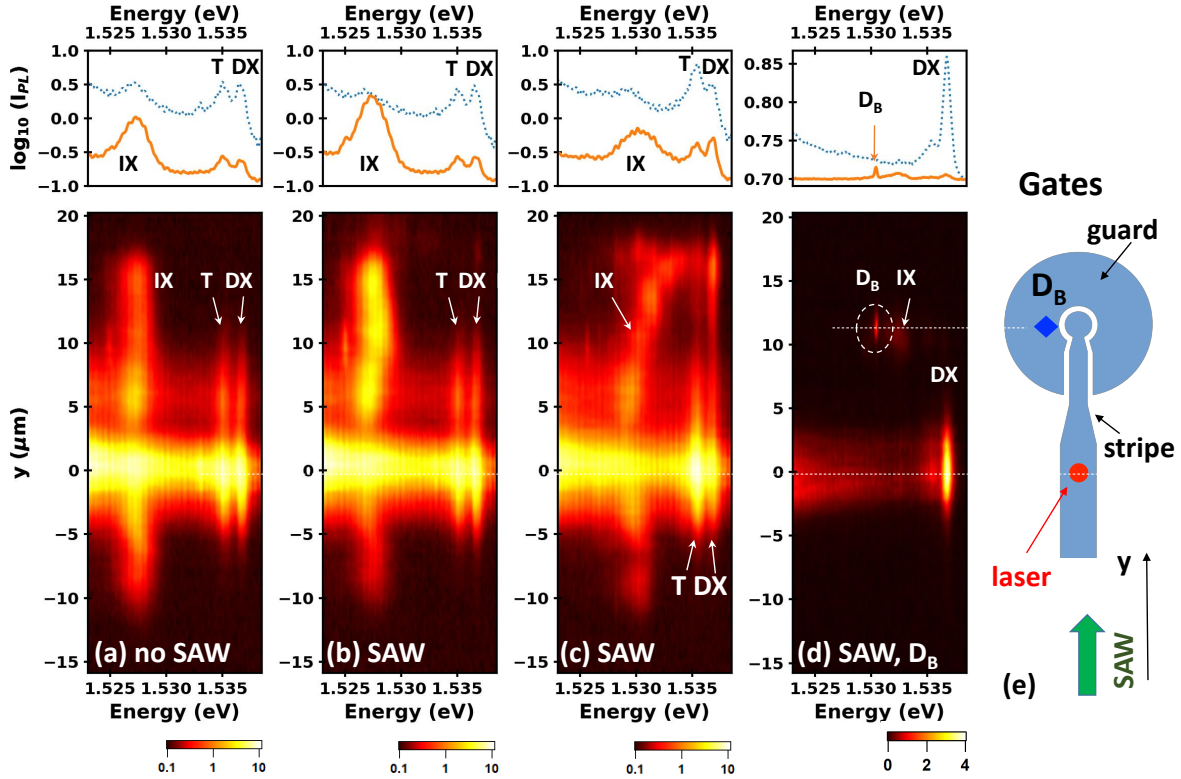


Figure 3: **Optically detected acoustic transport of IXs.** (Lower panels) Spatially resolved photoluminescence maps on a log intensity scale in the absence (a) and in the presence of a SAW for (b) $P_{\text{rf}} = -9$ dBm and $V_t = V_g = 0.2$ V and (c) $P_{\text{rf}} = -11$ dBm, for $V_t = 0.23$ V, and $V_g = 0.31$ V. (d) Corresponding map (linear color scale) with an impurity center D_B on the transport path and biasing conditions to enhance the impurity PL ($P_{\text{rf}} = -14$ dBm and $V_t = V_g = 0.4$ V). (e) Sketch of the transport path defined by electrostatic gates. The upper panels in (a)-(d) display profiles of the PL intensity integrated around the excitation region ($|y| < 3 \mu\text{m}$, blue dotted line) and along the transport path ($y > 3 \mu\text{m}$, orange solid line) on a log scale.

Here, the SAW amplitude and gate biasing conditions were selected to enhance the emission of a D_B center under the guard gate approx. $12 \mu\text{m}$ (corresponding to $15 \lambda_{\text{SAW}}$) away from the excitation spot (dashed circle).

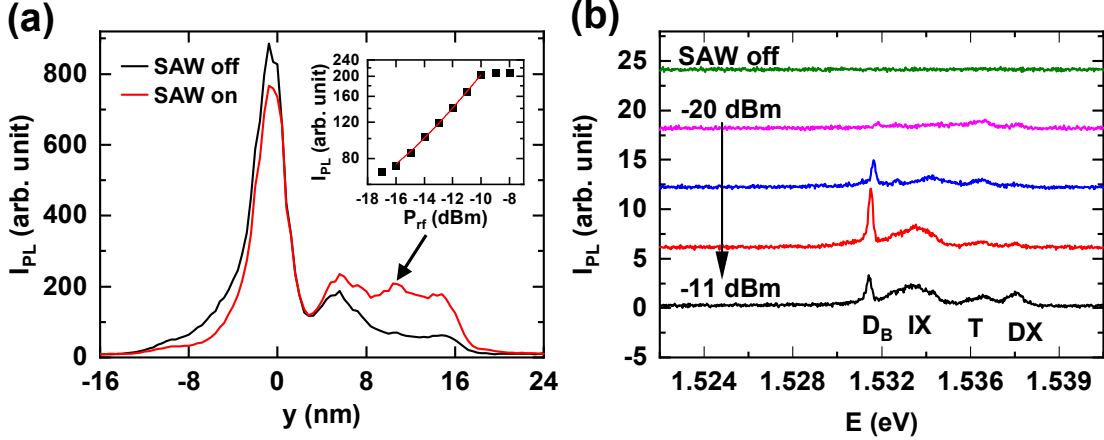


Figure 4: **Transport profiles and their power dependence.** (a) Energy-integrated cross-sections of the IX along the transport (y) direction in the absence [black, cf. Fig. 3(a)] and under a SAW [red, cf. Fig. 3(b)]. The profiles were obtained by integrating the emission over the IX energy range (from 1.5265 eV to 1.5308 eV). The acoustic transport enhances the IX PL intensity in the $+y$ direction and reduces it in the opposite direction. Inset: SAW power dependence of the remote IX PL (symbols) together with a linear fit (line). The PL was recorded at the position $y = 10.8 \mu\text{m}$ indicated by the arrow in the main plot. (b) PL spectra recorded for different acoustic powers P_{rf} around the remotely activated D_B at $y = 12 \mu\text{m}$ in Fig. 3(d). The PL intensity of the D_B is first enhanced and then suppressed with increasing SAW power.

A more detailed analysis of the IX SAW transport is presented in Fig. 4(a). The black and red curves in this figure compare PL profiles along transport path (y) recorded in the absence and presence of a SAW, respectively. In the absence of a SAW, the PL away from the excitation spot is attributed to the diffusion of the long living IXs. The acoustic transport along $+y$ significantly enhances the IX PL for $y > 8 \mu\text{m}$ and reduces it for $y < 0$. The inset of Fig. 4(a) displays the dependence of the remote IX PL on SAW power (P_{rf}). Here, the symbols correspond to the PL intensity recorded at the position indicated by the arrow in the main plot. The IX PL increase due to acoustic transport only becomes significant for P_{rf} above -16 dBm and saturates above -10 dBm . Within this transport window, the PL

intensity rises approximately linearly with SAW power, as shown by the line superimposed on the data points.

We now turn our attention to the dependence of the remote D_B emission on SAW power [(cf. Fig. 4(b)]. Here, the PL spectra were recorded by integrating the emission over a range $\Delta y = 6.4 \mu\text{m}$ around the D_B at $y = 12 \mu\text{m}$ in Fig. 3(d). In addition to the D_B line, the spectra also show emission features associated with IX, T, and the DX species. As in Fig. 3(d), most of the trions and DXs contributing to the spectra result not from acoustic transport but rather from the conversion from IXs. Interestingly, the remotely excited PL intensity from the D_B center first increases until it reaches a level comparable to the one observed for local excitation, and then becomes suppressed for higher SAW powers. This behavior indicates that SAWs can not only populate the D_B centers, but also depopulate them after a certain power threshold.

Photoluminescence dynamics and autocorrelation

The excitation of the D_B centers by GHz SAW fields induces a strong time modulation of their optical emission. The red line in Fig. 5(a) displays the time-resolved PL trace recorded on a D_B center located about $\ell \sim 8 \mu\text{m}$ away from the laser excitation spot. The blue curve reproduces, for comparison, the time-resolved profile of the exciting laser spot (not to scale), which consists of pulses with a FWHM of about 0.27 ns and a repetition time of 9 ns.

The short-period oscillations in the D_B response (red curve) correspond to the SAW period $T_{\text{SAW}} = 0.28 \text{ ns}$ demonstrating that the PL from these centers can follow the fast varying acoustic field. The pulses create a high density cloud of IX with long life time, which partially screens the SAW modulation potential around the excitation spot. As a consequence, within one T_{SAW} , only a fraction of the cloud is captured by the SAW, and the PL oscillations persist over times longer than the laser repetition period of 9 ns, since the IX cloud remains abundant. The envelope of the oscillations features two maxima: the first appears immediately after the laser pulse and the second at a delay of approximately

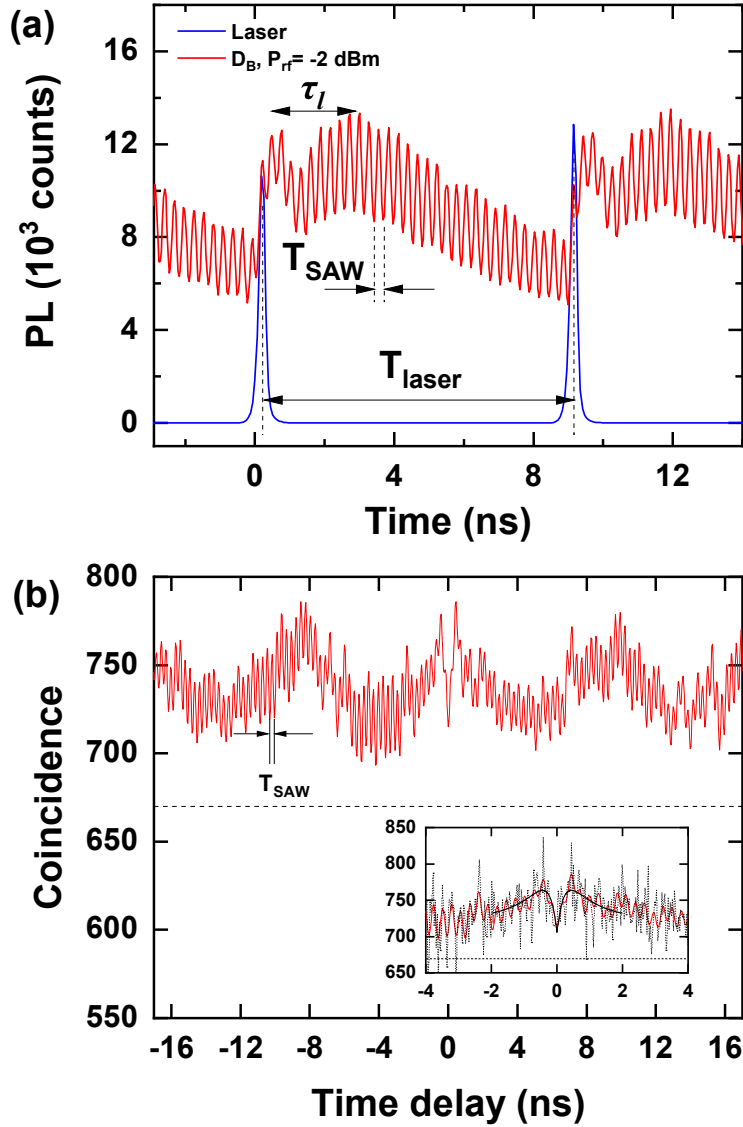


Figure 5: **Emission dynamics and photon autocorrelation from remote single D_B .** (a) Time-resolved PL from a D_B center pumped by IX transported by a $P_{\text{rf}} = -2$ dBm SAW (red). The IXs were photoexcited by a pulsed laser spot $8 \mu\text{m}$ away from the D_B center. T_{SAW} and T_{laser} denote the SAW period and laser repetition delay, respectively. τ_l indicates the SAW propagation time from the excitation spot to the D_B . The blue curve displays the corresponding profile for the laser pulses. (b) Second-order photon autocorrelation $g^{(2)}(\tau_c)$ for the same D_B center showing anti-bunching at zero delay (FFT filtered). The horizontal dashed line indicates the recorded background from IX emission close to the D_B center near zero time delay. The inset shows a close-up in the vicinity of zero time delay (dotted line: untreated; red: FFT-filtered) together with a fit to the time-dependence of the anti-bunching feature (black solid line, see text).

$\tau_\ell \sim 2.6$ ns (referencing the first maximum). The first maximum is attributed to the drift of hot excitons propelled by repulsive exciton interaction within the high-density cloud around the excitation spot.²² The second maximum is assigned to carriers transported by the SAW, which reach the D_B after a subsequent delay $\tau_\ell = \ell/v_{\text{SAW}}$, where $v_{\text{SAW}} = 2960$ m/s is the SAW velocity.

The photon emission statistics of the D_B center was addressed by recording photon autocorrelation $g^{(2)}$ histograms under acoustic excitation using a Hanbury-Brown and Twiss setup. The experiments were carried out by collecting the PL within a 3 nm spectral band around the D_B emission under a SAW excitation power $P_{\text{rf}} = -8$ dBm. The excitation laser spot was positioned $\ell \sim 8$ μm away. The histogram in the main plot of Fig. 5(b) displays the autocorrelation data after the application of a fast Fourier transform (FFT) filter (bandwidths explained in SI Sec. S3) to highlight the short modulation period at the SAW period T_{SAW} (red line): the corresponding untreated (raw) data is shown as a black dotted line in the inset as well as in SI Sec. S3. As in Fig. 5(a), the short and long period oscillations in the main plot of Fig. 5(b) are associated with modulation at the repetition periods T_{SAW} and T_{laser} of the SAW and the laser pulses, respectively. We note that the identification of the short-period SAW oscillations in the raw data (cf. inset) is very challenging since the required accumulation time (or, equivalently, total number of coincidences) increases as $(T_{\text{laser}}/T_{\text{SAW}})^2$. As a consequence, in order to achieve the same level of signal-to-noise ratio as reported in Ref. 23, where $T_{\text{SAW}} = 1.33$ ns and $T_{\text{laser}} = 25$ ns, the accumulation time would need to be 3 times higher for the SAW source investigated here, where $(T_{\text{laser}}/T_{\text{SAW}})^2 = 32^2$. The SAW induced oscillations become, nevertheless, clearly visible after FFT filtering. We show in Sec. S3 that the amplitude of the oscillations at T_{SAW} is over 20 dB above the noise floor.

The histograms of Fig. 5 show a distinct suppression of the coincidence rate at the time delay $\tau_c = 0$, a signature of photon anti-bunching. The black line in the enlarged area presented in the inset is a fit to the data of an exponential decay function together with a

Lorentzian that approximates the laser pulse profile (black solid line), from which we extract an autocorrelation recovery time $\tau_1 = 0.18 \pm 0.02$ ns (see details of the fit procedure in SI Sec. S3). τ_1 is much shorter than the PL decay time of the D_B centers of 0.8 ns measured in the absence of acoustic excitation (cf. Ref. 32). The short τ_1 indicates that pumping by high-frequency SAWs significantly reduces the emission time jitter due to the fast population followed by a fast depopulation of the center by the SAW field, thus reducing the time-interval available for recombination events. Similarly short response times (between 40 and 300 ps) have also been reported for GHz single-photon emitters in the form of electrically-driven quantum dots (QDs)^{35,36} as well as sources based on SAW-driven electron transport in lateral p-i-n diodes.²⁵

The PL collection bandwidth of 3 nm results in a relatively high autocorrelation background caused by IX emission around the D_B center. The background level in the coincidence count near $\tau_c = 0$ is recorded to be 670 ± 40 , as indicated by the horizontal dashed line. By taking into account this background correction, we estimate a second-order correlation at zero delay $g^2(0) = 0.41 \pm 0.21$, i.e., corresponding to an average anti-bunching level below the threshold of 1/2 for single-photon behavior. This level of anti-bunching is comparable to that reported for 1-GHz SAW-driven electron transport in lateral diodes.²⁵ The single-photon performance of D_B -based sources can be optimized by a better suppression of the spurious IX emission.

Discussion

In conclusion, we have investigated the dynamic modulation and transport of excitons by high-frequency, sub-micron-wavelength SAWs on GaAs DQW structures. In particular, we show that GHz-SAW field can pump single exciton states bound to impurities, which act as two level states emitting anti-bunched photons.

The centers can follow the high-frequency acoustic pumping rate leading to the emission

of anti-bunched photons synchronized with the SAW phase. The results thus demonstrate the feasibility of exciton manipulation as well as of exciton-based GHz single-photon sources using acoustic waves, the latter being a realization of high repetition rates in single-photon applications. Finally, multiple single exciton states can be excited by a single SAW beam, thus providing a pathway for scalable arrays of synchronized single-photon emitters.

Methods

Sample structure: The studies were carried out on an (Al,Ga)As DQW structure consisting of two coupled GaAs QWs grown by molecular beam epitaxy on a n-type doped GaAs(001) substrate [cf. Fig. 1(a)]. The QWs are 16 nm-wide and separated by a 4 nm-thick $\text{Al}_{0.33}\text{Ga}_{0.67}\text{As}$ barrier. The electric field F_z induced by the bias V_t applied across the structure drives photoexcited electrons into QW_2 and holes into QW_1 , thus increasing the recombination lifetime. Due to the narrow barrier width, the overlap of the electron and hole wavefunctions in the adjacent QWs is still sufficiently strong to maintain the Coulomb correlation required for IX formation. The DQW structure can thus hold both direct (or intra-QW, DX) and indirect (inter QW) excitons with transition energies indicated by the brown and green arrows in Fig. 1(a), respectively.

Generation of SAWs: SAWs with a wavelength of $\lambda_{\text{SAW}} = 800$ nm (corresponding to a SAW frequency $f_{\text{SAW}} = 3.58$ GHz at 4 K) were generated by split-finger aluminum interdigital transducers (IDTs) deposited on the sample surface [cf. Fig. 1(b)]. The depth of the DQW was chosen to yield a type II modulation under the SAW excitation.¹⁹ The IDTs are oriented along a $\langle 110 \rangle$ surface direction with a length and width of $150 \mu\text{m}$ and $28 \mu\text{m}$, respectively. The SAW intensity is quantified in terms of either the nominal radio-frequency (rf) power applied to the IDT (P_{rf}) or the SAW linear power density P_ℓ , which is defined as the ratio between the acoustic power and the width of the SAW beam. The latter is obtained by using the measured rf-scattering parameters of the IDTs to determine the fraction of the

input rf-power coupled to the acoustic mode.

Electrostatic channels for IX transport: The IX acoustic transport channel is defined by a semi-transparent Ti stripe placed on the SAW path and biased with a voltage V_t with respect to the doped substrate (cf. cross-section diagram of Fig. 1). The stripe is $2\ \mu\text{m}$ wide and ends on a small trap (diameter of $0.9\ \mu\text{m}$) surrounded by a guard gate with an external diameter of $7.5\ \mu\text{m}$. The guard gate, which is biased by a separate voltage V_g , reduces lateral stray electric fields in the narrow regions of the stripe, which can dissociate IXs.³⁷ As shown in the experiments, IX can easily tunnel over the small separation region (approx. $0.2\ \mu\text{m}$) between the stripe and guard gate.

Optical spectroscopy: Optically detected IX transport experiments were carried out at 4 K with a spatial resolution of approx. $1\ \mu\text{m}$. The excitons were excited by a spot from a pulsed laser (wavelength of 770 nm, pulse width of 270 ps) focused by a microscope objective on the semitransparent stripe. The photoluminescence (PL) from IXs emitted along the transport path is collected by the same objective and spectrally analysed by a monochromator (double for Fig. 2, single elsewhere.) with a charge-coupled-device (CCD) detector. Spatially and spectrally resolved PL maps of the IX distribution are obtained by aligning the transport path with the input slit of the spectrometer. The time-resolved PL studies were performed by triggering the laser pulses at a subharmonic ($f_{\text{SAW}}/32$) of the rf-frequency applied to the IDTs. The PL was in this case spectrally filtered by a $810 \pm 1.5\ \text{nm}$ band-pass filter (Semrock) and detected by a superconducting photon detector (Single Quantum) coupled to a time correlator (PicoQuant) with a combined time resolution of 40 ps. The data collection time for the autocorrelation measurement was 6 hours.

Acknowledgement

The authors thank M. Lopes and A. Hernández-Mínguez for helpful discussions and suggestions as well as S. Meister, S. Rauwerdink and A. Tahraoui for the expertise in sample

fabrication. S.T. and C.B. acknowledge financial support from the European Union Horizon 2020 research and innovation program under the Marie Skłodowska-Curie grant agreement No. 654603 and JSPS KAKENHI Grant Number 20H02559. M.Y., C.B. and P.V.S. acknowledge financial support from the French National Agency (ANR) and Deutsche Forschungsgesellschaft (DFG) in the frame of the the International Project on Collaborative Research SingleEIX Project No. ANR-15-CE24-0035/DFG SA-598-12/1.

References

- (1) Marcikic, I.; de Riedmatten, H.; Tittel, W.; Zbinden, H.; Gisin, N. Long-distance teleportation of qubits at telecommunication wavelengths. *Nature* **2003**, *421*, 509.
- (2) Bouwmeester, D.; Pan, J. W.; Mattle, K.; Eibl, M.; Weinfurter, H.; Zeilinger, A. Experimental quantum teleportation. *Nature* **1997**, *390*, 575.
- (3) Bouwmeester, D.; Pan, J.-W.; Daniell, M.; Weinfurter, H.; Zeilinger, A. Observation of Three-Photon Greenberger-Horne-Zeilinger Entanglement. *Phys. Rev. Lett.* **1999**, *82*, 1345–1349.
- (4) Bäuerle, C.; Glattli, D. C.; Meunier, T.; Portier, F.; Roche, P.; Roulleau, P.; Takada, S.; Waintal, X. Coherent control of single electrons: a review of current progress. *Rep. Prog. Phys.* **2018**, *81*, 056503.
- (5) Delsing, P. et al. The 2019 Surface Acoustic Waves Roadmap. *J. Phys. D* **2019**, *52*, 353001.
- (6) Bödefeld, C.; Wixforth, A.; Toivonen, J.; Sopanen, M.; Lipsanen, H. Pumping of Quantum Dots with Surface Acoustic Waves. *Phys. Status Solidi B* **2001**, *224*, 703.
- (7) Gell, J. R.; Ward, M. B.; Young, R. J.; Stevenson, R. M.; Atkinson, P.; Anderson, D.;

- Jones, G. A. C.; Ritchie, D. A.; Shields, A. J. Modulation of single quantum dot energy levels by a surface-acoustic-wave. *Appl. Phys. Lett.* **2008**, *93*, 081115.
- (8) Metcalfe, M.; Carr, S. M.; Muller, A.; Solomon, G. S.; Lawall, J. Resolved Sideband Emission of InAs/GaAs Quantum Dots Strained by Surface Acoustic Waves. *Phys. Rev. Lett.* **2010**, *105*, 037401.
- (9) Kinzel, J. B.; Rudolph, D.; Bichler, M.; Abstreiter, G.; Finley, J. J.; Koblmüller, G.; Wixforth, A.; Krenner, H. J. Directional and Dynamic Modulation of the Optical Emission of an Individual GaAs Nanowire Using Surface Acoustic Waves. *Nano Lett.* **2011**, *11*, 1512–1517.
- (10) Weiß, M.; Kinzel, J. B.; Schüle, F. J. R.; Heigl, M.; Rudolph, D.; Morkötter, S.; Döblinger, M.; Bichler, M.; Abstreiter, G.; Finley, J. J.; Koblmüller, G.; Wixforth, A.; Krenner, H. J. Dynamic Acoustic Control of Individual Optically Active Quantum Dot-like Emission Centers in Heterostructure Nanowires. *Nano Lett.* **2014**, *14*, 2256.
- (11) Hermelin, S.; Takada, S.; Yamamoto, M.; Tarucha, S.; Wieck, A. D.; Saminadayar, L.; Bäuerle, C.; Meunier, T. Electrons surfing on a sound wave as a platform for quantum optics with flying electrons. *Nature* **2011**, *477*, 435–438.
- (12) McNeil, R. P. G.; Kataoka, M.; Ford, C. J. B.; Barnes, C. H. W.; Anderson, D.; Jones, G. A. C.; Farrer, I.; Ritchie, D. A. On-demand single-electron transfer between distant quantum dots. *Nature* **2011**, *477*, 439–442.
- (13) Takada, S. et al. Sound-driven single-electron transfer in a circuit of coupled quantum rails. *Nat. Commun.* **2019**, *10*, 4557.
- (14) Gustafsson, M. V.; Aref, T.; Kockum, A. F.; Ekström, M. K.; Johansson, G.; Delsing, P. Quantum Acoustics: Propagating phonons coupled to a superconducting qubit. *Science* **2014**, *346*, 207.

- (15) Satzinger, K. J. et al. Quantum control of surface acoustic-wave phonons. *Nature* **2018**, *563*, 661–665.
- (16) Golter, D. A.; Oo, T.; Amezcua, M.; Stewart, K. A.; Wang, H. Optomechanical Quantum Control of a Nitrogen-Vacancy Center in Diamond. *Phys. Rev. Lett.* **2016**, *116*, 143602.
- (17) Golter, D. A.; Oo, T.; Amezcua, M.; Lekavicius, I.; Stewart, K. A.; Wang, H. Coupling a Surface Acoustic Wave to an Electron Spin in Diamond via a Dark State. *Phys. Rev. X* **2016**, *6*, 041060.
- (18) Whiteley, S. J.; Wolfowicz, G.; Anderson, C. P.; Bourassa, A.; Ma, H.; Ye, M.; Koolstra, G.; Satzinger, K. J.; Holt, M. V.; Heremans, F. J.; Cleland, A. N.; Schuster, D. I.; Galli, G.; Awschalom, D. D. Spin-phonon interactions in silicon carbide addressed by Gaussian acoustics. *Nat. Phys.* **2019**, *15*, 490–495.
- (19) Rudolph, J.; Hey, R.; Santos, P. V. Long-range Exciton Transport by Dynamic Strain Fields in a GaAs Quantum Well. *Phys. Rev. Lett.* **2007**, *99*, 047602.
- (20) Lazić, S.; Violante, A.; Cohen, K.; Hey, R.; Rapaport, R.; Santos, P. V. Scalable interconnections for remote indirect exciton systems based on acoustic transport. *Phys. Rev. B* **2014**, *89*, 085313.
- (21) Violante, A.; Cohen, K.; Lazić, S.; Hey, R.; Rapaport, R.; Santos, P. V. Dynamics of indirect exciton transport by moving acoustic fields. *New J. Phys.* **2014**, *16*, 033035.
- (22) Violante, A.; Hey, R.; Santos, P. V. Coherent transport and manipulation of spins in indirect-exciton nanostructures. *Phys. Rev. B* **2015**, *91*, 125302.
- (23) Couto, Jr., O. D. D.; Lazić, S.; Iikawa, F.; Stotz, J.; Hey, R.; Santos, P. V. Photon anti-bunching in acoustically pumped quantum dots. *Nat. Photonics* **2009**, *3*, 645.

- (24) Hernández-Mínguez, A.; Möller, M.; Breuer, S.; Pfüller, C.; Somaschini, C.; Lazić, S.; Brandt, O.; García-Cristóbal, A.; de Lima, M. M.; Cantarero, A.; Geelhaar, L.; Riechert, H.; Santos, P. V. Acoustically Driven Photon Antibunching in Nanowires. *Nano Lett.* **2012**, *12*, 252.
- (25) Hsiao, T.-K.; Rubino, A.; Chung, Y.; Son, S.-K.; Hou, H.; Pedrós, J.; Nasir, A.; Éthier-Majcher, G.; Stanley, M. J.; Phillips, R. T.; Mitchell, T. A.; Griffiths, J. P.; Farrer, I.; Ritchie, D. A.; Ford, C. J. B. Single-photon emission from single-electron transport in a SAW-driven lateral light-emitting diode. *Nat. Commun.* **2020**, *11*, 917.
- (26) Sogawa, T.; Santos, P. V.; Zhang, S. K.; Eshlaghi, S.; Wieck, A. D.; Ploog, K. H. Transport and lifetime enhancement of photoexcited spins in GaAs by surface acoustic waves. *Phys. Rev. Lett.* **2001**, *87*, 276601.
- (27) Hernández-Mínguez, A.; Biermann, K.; Lazić, S.; Hey, R.; Santos, P. V. Kerr detection of acoustic spin transport in GaAs (110) quantum wells. *Appl. Phys. Lett.* **2010**, *97*, 242110.
- (28) Sanada, H.; Sogawa, T.; Gotoh, H.; Onomitsu, K.; Kohda, M.; Nitta, J.; Santos, P. V. Acoustically Induced Spin-Orbit Interactions Revealed by Two-Dimensional Imaging of Spin Transport in GaAs. *Phys. Rev. Lett.* **2011**, *106*, 216602.
- (29) Bertrand, B.; Hermelin, S.; Takada, S.; Yamamoto, M.; Tarucha, S.; Ludwig, A.; Wieck, A. D.; Bäuerle, C.; Meunier, T. Fast spin information transfer between distant quantum dots using individual electrons. *Nat. Nanotechnol.* **2016**, *11*, 672–676.
- (30) Jadot, B.; Mortemousque, P.-A.; Chanrion, E.; Thiney, V.; Ludwig, A.; Wieck, A. D.; Urdampilleta, M.; Bäuerle, C.; Meunier, T. Distant spin entanglement via fast and coherent electron shuttling. *Nat. Nanotechnol.* **2021**, <https://doi.org/10.1038/s41565-021-00846-y>.

- (31) Schinner, G. J.; Repp, J.; Schubert, E.; Rai, A. K.; Reuter, D.; Wieck, A. D.; Govorov, A. O.; Holleitner, A. W.; Kotthaus, J. P. Confinement and Interaction of Single Indirect Excitons in a Voltage-Controlled Trap Formed Inside Double InGaAs Quantum Wells. *Phys. Rev. Lett.* **2013**, *110*, 127403.
- (32) Yuan, M.; Hernández-Mínguez, A.; Biermann, K.; Santos, P. V. Tunneling blockade and single-photon emission in GaAs double quantum wells. *Phys. Rev. B* **2018**, *98*, 155311.
- (33) de Lima, Jr., M. M.; Santos, P. V. Modulation of photonic structures by surface acoustic waves. *Rep. Prog. Phys.* **2005**, *68*, 1639.
- (34) Sogawa, T.; Santos, P. V.; Zhang, S. K.; Eshlaghi, S.; Wieck, A. D.; Ploog, K. H. Dynamic band-structure modulation of quantum wells by surface acoustic waves. *Phys. Rev. B* **2001**, *63*, 121307.
- (35) Hargart, F.; Kessler, C. A.; Schwarzbäck, T.; Koroknay, E.; Weidenfeld, S.; Jetter, M.; Michler, P. Electrically driven quantum dot single-photon source at 2 GHz excitation repetition rate with ultra-low emission time jitter. *Appl. Phys. Lett.* **2013**, *102*, 011126.
- (36) Schlehahn, A.; Schmidt, R.; Hopfmann, C.; Schulze, J.-H.; Strittmatter, A.; Heindel, T.; Gantz, L.; Schmidgall, E. R.; Gershoni, D.; Reitzenstein, S. Generating single photons at gigahertz modulation-speed using electrically controlled quantum dot microlenses. *Appl. Phys. Lett.* **2016**, *108*, 021104.
- (37) Schinner, G. J.; Schubert, E.; Stallhofer, M. P.; Kotthaus, J. P.; Schuh, D.; Rai, A. K.; Reuter, D.; Wieck, A. D.; Govorov, A. O. Electrostatically trapping indirect excitons in coupled $\text{In}_x\text{Ga}_{1-x}\text{As}$ quantum wells. *Phys. Rev. B* **2011**, *83*, 165308.

Supporting Information to:

Remotely Pumped GHz Antibunched Emission from Single Exciton Centers in GaAs

Mingyun Yuan¹, Klaus Biermann¹, Shintaro Takada², Christopher Bäuerle³, and Paulo V. Santos¹

¹*Paul-Drude-Institut für Festkörperelektronik, Leibniz-Institut im Forschungsverbund Berlin e. V., Hausvogteiplatz 5-7, 10117 Berlin, Germany*

²*National Institute of Advanced Industrial Science and Technology (AIST), National Metrology Institute of Japan (NMIJ), 1-1-1 Umezono, Tsukuba, Ibaraki 305-8563, Japan*

³*Univ. Grenoble Alpes, CNRS, Grenoble INP, Institut Néel, 38000 Grenoble, France*

Calculation of the SAW-induced energy modulation

We calculate in this section the bandgap modulation induced by the SAW. For that purpose, we compare the measured electrical response of the IDTs with numerical calculation of the SAW fields carried out by solving the elasticity equations for the layer structure of the sample.³³ Fig. S1 displays the rf scattering coefficient S_{11} measured for the IDT, which yields the fraction of the applied rf power reflected by the transducers. From the amplitude of the dip at the resonance frequency $f_{\text{SAW}} = 3.54$ GHz, we extract that for a typical applied power of 30 W/m, the transmitted SAW power propagating along one direction of the IDT is $P_\ell = 0.4$ W/m. The SAW strain modulates the energy of both the conduction, E_e and the valence bands (heavy hole), E_{hh} . The calculated combined bandgap modulation $E_e - E_{hh}$ at the depth of the DQW is shown in Fig. S2(a). We plot in Fig. S2(b) the calculated piezoelectric energy E_p in the DQW plane underneath the metal gates. For high SAW amplitudes, this field can dissociate excitons, thus inducing a quenching of the PL.

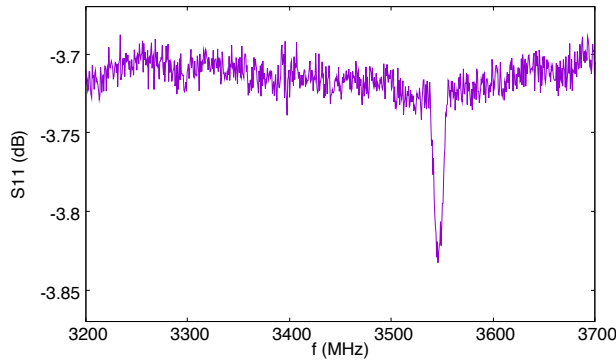


Figure S1: Radio-frequency scattering parameter S_{11} (corresponding to the electric reflection coefficient) measured at room temperature for the IDT used to generate the SAWs in the experiments.

Acoustic modulation of the transition energies

In addition to the studies of the dependency of the bound exciton linewidths on acoustic intensity, we also investigated how the acoustic fields impact the DX and trion lines.

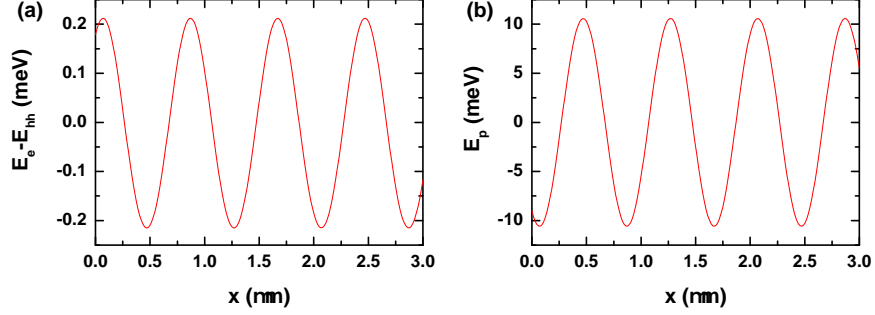


Figure S2: (a) Strain-induced bandgap modulation $E_e - E_{hh}$ at the depth of the DQW calculated for $P_\ell = 0.4$ W/m. (b) The corresponding piezoelectric energy E_p .

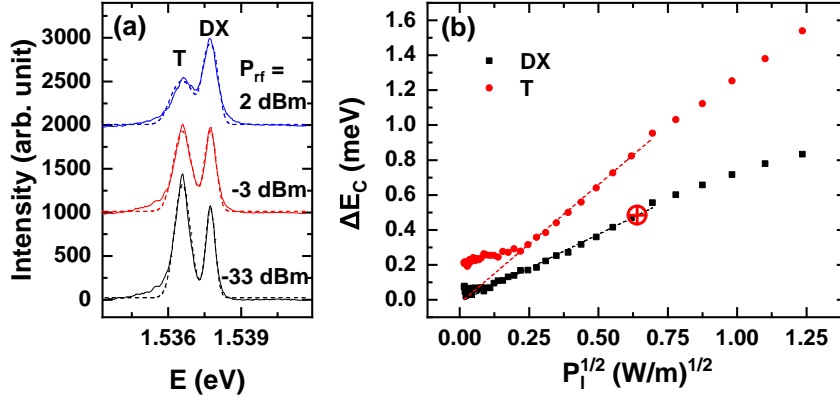


Figure S3: (a) (symbols) Time-averaged photoluminescence (PL) spectra recorded under flat-band conditions for different rf-acoustic powers P_ℓ applied to the IDT. DX and T denote that direct exciton and trion transitions, respectively. The superimposed curves are fits to Eq. (S1). (b) SAW modulation amplitude ΔE_C ($C = \text{DX, T}$, solid symbols) vs. $\sqrt{P_\ell}$. The dashed lines are linear fits for low SAW intensities.

Figure S3(a) displays PL spectra recorded under flat-band conditions for increasing SAW intensities (quantified by the nominal power P_{rf} applied to the IDT). Each spectrum displays two lines associated with the excitation of DXs and trions (T, a DX bound to a free carrier, studied in Ref. 32). The spectrum for the lowest P_{rf} essentially corresponds to the PL response in the absence of acoustic excitation. With increasing SAW intensity, both lines slightly broaden and the overall emission intensity decreases.

In order to extract the effects of the acoustic field, we assume that PL lines have a Gaussian shape with width w and that their central energy is modulated by the SAW according to Eq. (1) of the main text. Under these assumptions, the time-integrated PL spectrum can be expressed by the following integral over one SAW period

$$I_C(E) = \frac{1}{T_{\text{SAW}}} \frac{I_{C,0}}{w\sqrt{\pi/2}} \int_0^{T_{\text{SAW}}} \exp \left[-2 \left(\frac{E - E_C(t)}{w} \right)^2 \right] dt. \quad (\text{S1})$$

For energy shifts $\Delta E_C \ll w$, the modulation manifests itself as a broadening of the lines with increasing SAW amplitude. For high modulation amplitudes, the time-averaged PL line splits into two peaks with energies $E_{C,0} \pm \Delta E_C/2$ corresponding to the maximum and minimum band-gaps under the SAW field.

The lines superimposed on Fig. S3(a) are fits of the measured PL data to Eq. S1. From the fit we extract the SAW modulation amplitudes ΔE_C for DX and trion, plotted as symbols in Fig. S3(b) for different SAW amplitudes. The latter is quantified in terms of the SAW linear power density P_ℓ , defined as the acoustic power carried by the SAW mode per unit length perpendicular to the SAW beam. The expected linear dependence on $\sqrt{P_\ell}$ is revealed when the SAW-induced apparent broadening exceeds the unperturbed (i.e., in the absence of a SAW) width of the PL line, as shown by the dashed lines. For $P_\ell^{1/2} > 0.7 \text{ (W/m)}^{1/2}$ one observes a nonlinear increase of ΔE_C with SAW amplitude.

The modulation amplitude determined from the fits for DX (square) correlates well with the band-gap modulation expected from the deformation potential mechanism shown in Fig. . As an example, the circled red cross in Fig. S3b marks ΔE_C for $P_\ell = 0.4 \text{ W/m}$ from the

calculation. In contrast, ΔE_C for trion (circle) deviates significantly from the calculation. It indicates that the simple model of adding the respective modulation of the conduction band and the valance band, used for the calculation here, is not suitable for trion due to the binding to an extra charge.

Background correction of the autocorrelation data

In Fig. S4(a) we show the untreated second-order autocorrelation data $g^{(2)}$. Resolving features at frequencies as high as $f_{\text{SAW}} = 3.58$ GHz is very challenging for the second-order autocorrelation measurement. To verify the oscillations at f_{SAW} , we perform fast Fourier transform (FFT) to the data and the FFT spectrum is shown in Fig. S4(b). The peak corresponding to f_{SAW} is very significant, with a signal level more than 20 dB above the noise floor, confirming the SAW modulation. Also at a comparable level is the peak resulting from the laser frequency.

Subsequently, we filter away certain bandwidths in the FFT spectrum, indicated by the brackets in Fig. S4(b) to improve the signal-to-noise ratio. The time constant τ_1 (see value in the bottom paragraph) of the antibunching feature translates into the frequency of $f_1 = 1/2\pi\tau_1 = 0.88$ GHz. We filter out noise above 1.5 times of this frequency with the exception of the narrow bandwidth around the SAW frequency. By choosing this filtering approach we preserve the antibunching feature, resolve the SAW modulation and reject the high-frequency random noise. The filtered data is presented in Fig. 5(b) of the main text.

To estimate the background emission from IXs, we diverted the detection spot away from the D_B center to a position, where the PL from the center disappeared but the IX signal remained similar. A background autocorrelation count $[C_{\text{bgd}}]^2$ was recorded at this position. The measured total count $[C_{\text{total}}]^2$ can be expressed as $[C_{\text{bgd}} + C_{\text{center}}]^2$, where $[C_{\text{center}}]^2$ is the count from the D_B center that is sought after. From the measurements we extract $[C_{\text{bgd}}]^2 + 2C_{\text{bgd}}C_{\text{center}} \approx 0.85[C_{\text{total}}]^2$. The corresponding level for the zero-time delay

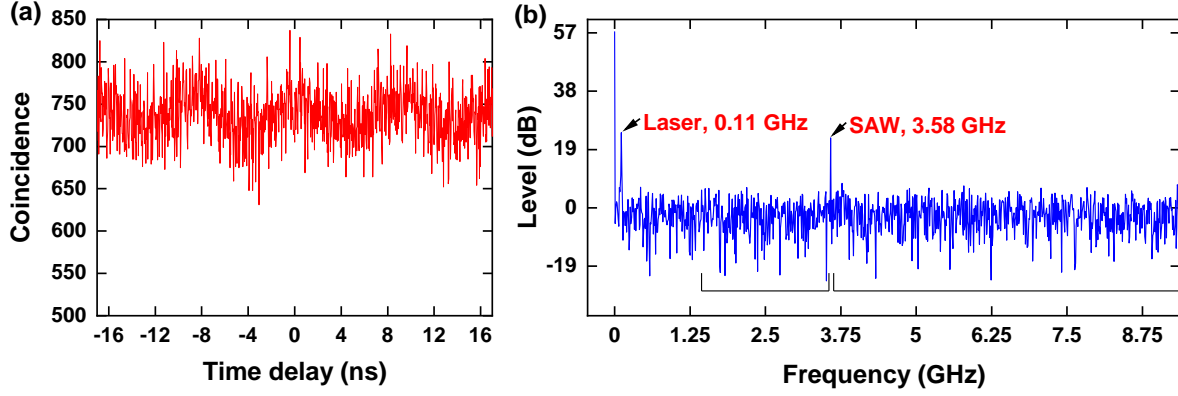


Figure S4: Autocorrelation data processing. (a) Untreated data. (b) FFT spectrum of data presented in (a), showing peaks at the laser frequency and the SAW frequency. The brackets at the bottom indicate the filtered-away bandwidths in Fig. 5(b) of the main text.

is indicated as the dashed lines in Fig. 5(b) in the main text.

The anti-bunching feature is fitted to a function of the time delay τ_c :

$$Coincidence = h_1 - b \exp\left(-\frac{|\tau_c|}{\tau_1}\right) + h_2 \left[\frac{1}{1 + (2\tau_c/w)^2} - 1 \right], \quad (S2)$$

comprised of an exponential decay with a magnitude of b and a time constant of τ_1 , and a Lorentzian with a FWHM of w to approximate the laser-induced pulse profile. The offsets $h_1 = 780$ and $h_2 = 60$ are treated as constants. The fitted parameters are $b = 74 \pm 6$, $\tau_1 = 0.18 \pm 0.02$ ns and $w = 2 \pm 0.08$ ns.